PAPER

Check for updates

Open micro-combinatorial analysis systems of crystal growth critical points of a π-conjugated molecule in ionic liquid nanoliter droplets†

Satoshi Watanabe, [ID] *[a] Shun Inouchi[b] and Masashi Kunitake [ID] [c]

Crystal engineering methodologies based on reproducible and high-throughput fabrication of high-quality single crystals have attracted much attention. Crystal formation and growth are governed by crystal growth theory. The driving force of crystallization is systematically represented with phase diagrams. However, constructing phase diagrams usually requires relatively large quantities of samples (milligrams to grams) and substantial time (weeks to months) to evaluate many conditions. Therefore, an easy and quick methodology to obtain phase diagrams, revealing critical conditions for valuable samples, is required. Here, we proposed a new method to obtain phase diagrams based on nanoliter droplet arrays of nonvolatile ionic liquids prepared by inkjet printing. Anthracene derivatives and 1-octyl-4-methylpyridinium derivatives were used as the solute and solvent, respectively. Optimization of ejection conditions, such as applied voltage, frequency, pulse width, and head temperature, enabled the formation of a 0.5 nL droplet per ejection. Inkjet printing under these conditions formed nanodroplet arrays on substrates at a droplet-patterned density of *ca.* 50 dots per cm². The volume of each patterned droplet was varied from 10 to 100 nL by changing the number of ejections. The dissolution temperature of anthracene at each concentration was obtained at a heating rate of 0.2 °C min⁻¹. This heating rate was found to be 10 times faster than the conventional technique. The same phase diagram as that prepared by the conventional technique was obtained in the range of 75–300 mM. The standard deviation of the dissolution temperatures was 0.8 °C (2.5%). This technique will facilitate the crystallization of multiple and valuable samples.

Introduction

Crystal engineering of small molecules has attracted much attention for X-ray single-crystal analysis to determine crystal structures[1–5] and for enhancing their physical properties, such as carrier mobilities in organic field-effect transistors,[6–8] upconversion luminescence,[9,10] actuation by photo-isomerization,[6,7] texture in chocolates,[8,9] and medicinal efficacy of medicines.[10,11] Success in these applications requires high-quality single crystals. Crystal qualities are classified into crystallinity (single or polycrystals), crystal size and shape, anisotropic orientation, and crystal purity (densities of impurities and/or defects). The method of fabrication is pertinent to enhancing the crystal quality.

ªDivision of Applied Chemistry and Biochemistry, National Institute of Technology, Tomakomai College, Nishikioka 443, Tomakomai, Hokkaido 059-1275, Japan. E-mail: watasato@tomakomai-ct.ac.jp

ᵇGraduate School of Science and Technology, Kumamoto University, 2-39-1 Kurokami, Chuo-ku, Kumamoto City, Kumamoto 860-8555, Japan

ᶜInstitute of Industrial Nanomaterials, Kumamoto University, 2-39-1 Kurokami, Chuo-ku, Kumamoto City, Kumamoto 860-8555, Japan

† Electronic supplementary information (ESI) available. See DOI: https://doi.org/10.1039/d5ra00170f

Crystal fabrication techniques are broadly divided into dry and wet processes.[12,13] Wet processes, sometimes termed "solution processes", are often used for organic compounds because they do not sublimate or decompose at low temperatures and in the air. Crystals form by facilitating crystallization from homogeneous solutions by solvent evaporation, cooling, introducing a poor solvent or using precipitating agents.[14–16] In the initial stages of research, experimental conditions for crystallization are determined by trial and error, yet the crystal growth conditions remain ambiguous. However, this strategy often fails to form crystals and/or lacks reproducibility because the causal relationship between crystal formation and experimental conditions remains unclear.

Classical crystal growth theory indicates that crystal growth is governed by nucleation and crystal growth, which depend on concentration and temperature.[17,18] The driving forces of nucleation and crystal growth are quantitatively calculated by obtaining the difference in temperature and concentration from the dissolution and precipitation curves in phase diagrams. That is why the dissolution and precipitation curves are often termed critical curves of crystal growth and nucleation, respectively. In addition, phase diagrams indicate the specific crystallization conditions of a molecule. This study reports that the nucleation conditions of organic semiconductor molecules change between the air/liquid

interface and the bulk solution phase.[19] This is because of the Gibbs absorption of molecules at the air/liquid interface. This knowledge facilitates crystal growth based on the phase diagrams of organic semiconductors.[20] Obtaining phase diagrams is the first step to obtaining high-quality crystals with good reproducibility. However, obtaining a phase diagram requires milligram- or gram-scale reagents and times ranging from 1 week to nearly 1 month. This hinders the acquisition of phase diagrams for valuable reagents, such as nucleic acids, proteins, and synthesized compounds, as well as the application of various conditions, such as good solvents, poor solvents, salts, and pH.

Microanalysis and synthesis in small well plates are performed because of their high throughput based on low material consumption, high reaction efficiency, and ease of environmental control.[21–31] Zheng *et al.* screened protein crystallization conditions by microfluidic chip mixing with several nanoliter solutions.[30] Tyler *et al.* reported a new screening technique of crystallization conditions for crystal polymorphs of small organic molecules by evaporating nanoliter solutions covered with oils.[31] Knowles *et al.* succeeded in obtaining condensed phase diagrams of biomolecules on combinatorial microdroplets.[32] We reasoned that if solubilities are observed in nanoliter droplets, many dissolution curves can be obtained concomitantly with only a small quantity of reagent. However, the concentration of nanoliter droplets is difficult to determine during evaporation because of their small size and rapid evaporation speed. This disadvantage hinders the possibility of extending microsystems to open ones, not just to crystal engineering.

In this study, we demonstrate a new open micro analysis system that can obtain the crystal-solution phase diagram of a small molecule in nanoliter droplet arrays of an ionic liquid prepared with a piezo-type inkjet printer. Ionic liquids are nonvolatile in air; thus, even nanoliter droplets can easily maintain a constant concentration. Ionic liquids are used to crystallize,[33–35] electrochemically decompose,[36] and assemble two-dimensional materials.[37] As solutes and ionic liquids, anthracene derivatives and 1-octyl-4-methylpyridinium derivatives were used. Anthracene derivatives were well known as a typical π-conjugated molecule, and anthracene was used mainly in this study owing to its basic chemical structure and high solubility in ionic liquids. 1-Octyl-4-methylpyridinium derivatives were some of the ionic liquids that dissolved anthracene derivatives well.[38]

Materials and methods

Materials

Anthracene, 9,10-dibromoanthracene, and 1-octyl-4-methylpyridinium bis(trifluorosulfonyl)imide (pC8PryC1 TFSA) were obtained from FUJIFILM Wako Pure Chemical. 1-Octyl-4-methylpyridinium bis(trifluorosulfonyl)imide (pC8PryC1 FSA) was obtained from DKS. o-Dichlorobenzene (DCB) was purchased from the Tokyo Chemical Industry.

Ejection condition

Anthracene was dissolved in DCB at 100 mM. Prior to inkjet ejection, the anthracene solutions and pC8PryC1 FSA were

passed through a polytetrafluoroethylene filter (pore size: 0.2 μm) and then added into 1 mL-volume sample vials. The vials were set in a piezoelectric inkjet printer (LaboJet-500, MICRO-JET, Japan) equipped with an IJHB-1000 thermal heating head. The distance between the head tip and glass substrates was 1–2 mm. The solution and ionic liquid were ejected under air at *ca.* 25 °C. The ejections were adjusted by changing the voltage (0–80 V), pulse width (40–120 μs), and frequency (120–500 Hz) applied to the piezo devices attached to the head. The head temperature was set to 30 °C for the anthracene solution and 40 °C for the ionic liquid. The ejected droplets were observed with a video camera and a strobe light synchronized with the ejected frequency. The flight velocity of the ejected droplets was calculated from the droplet position in the camera image and strobe delay time. The volume of the droplet was determined by dividing the mass of the solutions (*ca.* 10 μL obtained by 20 000 ejections) by the density of DCB (1.30 g cm^{-3}) or pC8PryC1 FSA (1.27 g cm^{-3}).

Printing and observation

Fig. 1a–d shows the preparation protocol for a droplet array consisting of anthracene in an ionic liquid by inkjet printing for the simultaneous screening and construction of a phase diagram. Flat glass substrates (10 mm × 10 mm × 0.2 mm) were cleaned by ultrasonication in acetone and chloroform for 20 min each. Anthracene solution was ejected at the 1 × 1 and 3 × 3 array positions onto the glass substrates under optimized conditions (Fig. 1a). The solution was air-dried because heating or vacuum caused sublimation of the anthracene from the substrates. The anthracene solution was again ejected onto the same location of the substrates until a predetermined quantity of anthracene was obtained (Fig. 1b). After air-drying, 10–100 nL of pC8PryC1 FSA was ejected to cover the anthracene (Fig. 1c). The concentration of anthracene in each droplet was controlled by changing the quantity (droplet number) of the anthracene solution ejected.

The substrates were placed on an SS053-convex glass heating table (BLAST, Japan). The accuracy of the temperature control was ±0.5 °C. The substrates were observed in transmission mode using an optical digital microscope (RX-100) equipped with a high-resolution HR-5000 lens (HIROX, Japan). The lens (with a camera) was above the samples, and white light was irradiated from the bottom of the samples. The samples were heated at rates from 0.1 °C min^{-1} to 1.0 °C min^{-1} until the crystals dissolved completely (Fig. 1d).

Conventional method

Anthracene and pC8PryC1 FSA were added to 1 to 2 mL vials at 75, 150, and 300 mM. The vials were set on an aluminium block on a PH121 temperature-tuned table controlled with a PCC-117-Co controller. The precision of the temperature control was ±0.1 °C. The heating rates of the samples were from 0.0080 °C min^{-1} to 0.20 °C min^{-1}. Crystal dissolution was determined visually.
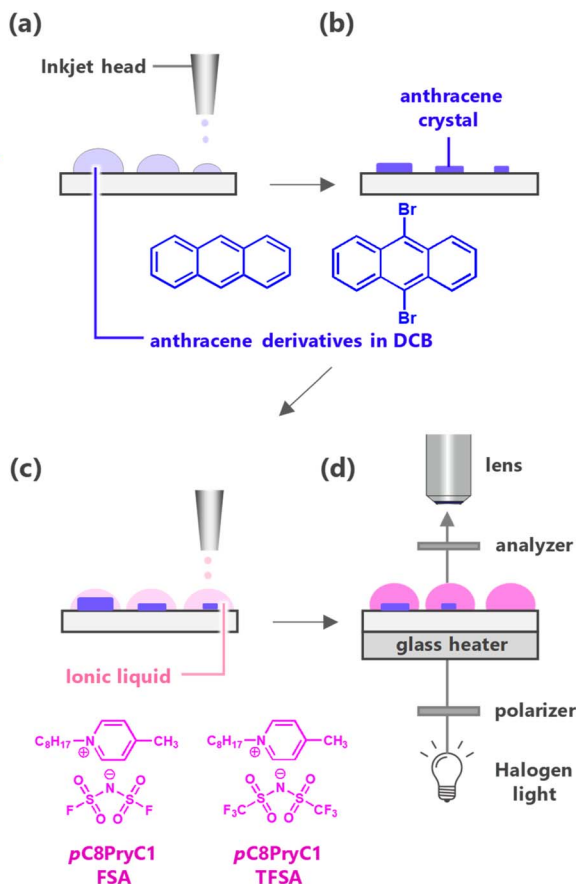
Fig. 1 Schematic for preparing a dot array, consisting of anthracene in an ionic liquid, by inkjet printing for simultaneous screening and construction of a phase diagram. (a) Printing of anthracene in DCB solution, (b) formation of anthracene crystals after air drying, (c) printing of pC8PryC1 derivatives on anthracene derivative crystals, and (d) microscopy observation of anthracene crystal dissolution at the heating stage.

Results

Ejection conditions of anthracene/o-dichlorobenzene solution and pC8PryC1 FSA

First, the optimized ejection conditions of the anthracene solutions and the neat ionic liquid were studied. Fig. 2a–d shows the flying velocity and/or volume of a droplet plotted against (a and b) pulse width and (c and d) applied voltage in (a and c) anthracene solutions and (b and d) pC8PryC1 FSA. The optimized ejection conditions enabled stable ejection of nanodroplets (0.5 nL per ejection) of anthracene solution and the ionic liquid. As shown in Fig. 2a and b, the droplet velocities of the anthracene solution and ionic liquid were maximized at pulse widths of 78 and 75 µs, respectively. The maximum droplet velocities at 5–6 m s^{-1} were obtained at an applied voltage of 20 V for the anthracene solution and 50 V for the ionic liquid. As depicted in Fig. 2c and d, the velocity and volume of a droplet of the anthracene solutions and ionic liquid were proportional to the applied voltage at the same pulse width (75 µs). The droplets were stably ejected at 20–50 V for the anthracene solutions and at 50–55 V for the ionic liquid. The ejection
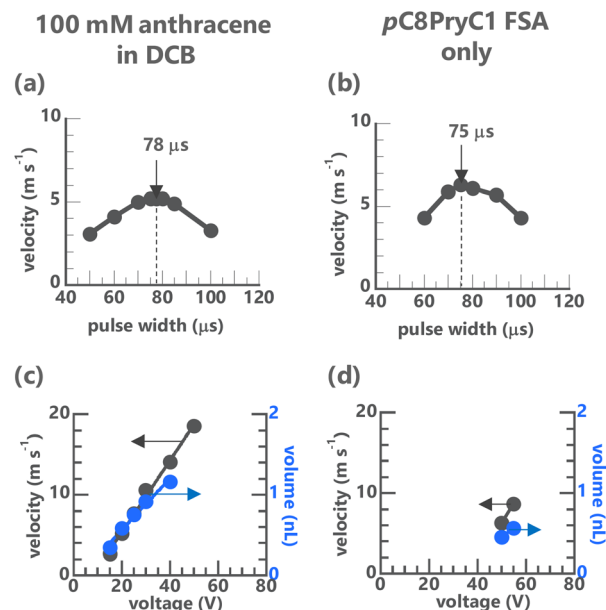

Fig. 2 Flying velocity of droplets plotted against the pulse width of applied voltages in (a) 100 mM anthracene in DCB and (b) pC8PryC1 FSA. Flying velocity (gray) of droplets and volume (blue) of droplets plotted against applied voltages in (c) 100 mM anthracene in DCB and (d) pC8PryC1 FSA. The frequency of applied voltages and the temperature of the inkjet head were 500 Hz and 30 °C for anthracene, and 120 Hz and 40 °C for pC8PryC1 FSA, respectively. The applied voltages were fixed at 20 V in (a) and 50 V in (b). The pulse width was set at 75 µs in (c) and (d). The volume of a droplet was obtained by dividing the weight of 20 000 droplets by the density of (c) DCB and (d) pC8PryC1 FSA.

conditions were chosen to be 0.60 nL at 20 V for the anthracene solution and 0.56 nL at 55 V for the ionic liquid. The average volume and standard deviation of the droplets ejected 10× were 0.595 and 0.0171 nL (0.3%) for the anthracene solutions and 0.524 and 0.0369 nL (7.0%) for the ionic liquid, respectively (Table S1†).

The flight velocities and ejection volumes of droplets are determined by the head types, ejection conditions, and the ink properties of surface tension and viscosity. The influence of the ink viscosity was particularly large. The viscosity of the ionic liquid (34 mPa s at 40 °C) was *ca.* 30× higher than that of *o*-dichlorobenzene (DCB; 1.32 mPa s at 25 °C). The applied voltages for the ionic liquid must be higher than those for the anthracene solutions. Ionic liquids were difficult to stably eject at temperatures <40 °C, at frequencies higher than 120 Hz, without an applied voltage of 50–55 V. Low-viscosity ionic liquids at high temperatures form stable flying droplets but completely dissolve anthracene crystals when the ionic liquids are covered on a small quantity of anthracene crystals on substrates. This is not suitable for measuring dissolution temperature by observing the phase transition from the heterogeneous crystal coexistence phase to the homogeneous solution phase.

Nanoliter droplets patterned on substrates

First, 51 nL of anthracene in DCB was placed on the substrate, *i.e.*, 0.91 µg (5.1 nmol) of anthracene at 25 °C. Fig. 3a shows an
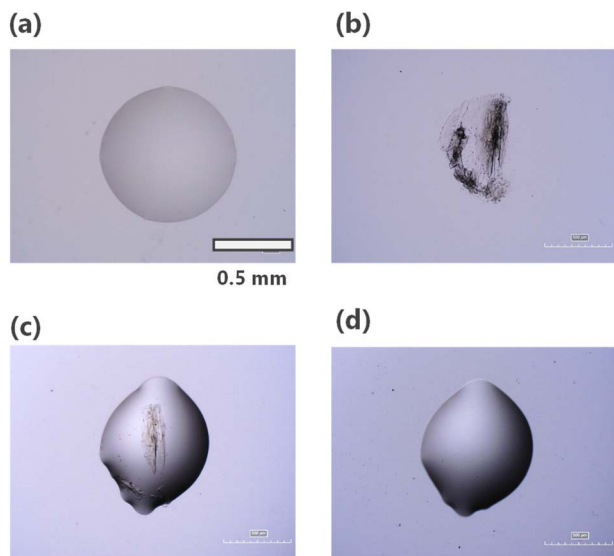
Fig. 3 Optical microscope images of a glass substrate obtained at each step of preparing a nanoliter solution. (a) Anthracene (51 nL) in DCB at 100 mM by inkjet printing (frequency: 500 Hz, pulse width: 75 μs, head temperature: 30 °C, applied voltage: 20 V, number of ejections: 86); (b) after air drying for several hours to evaporate DCB [0.91 μg (5.1 nmol) of anthracene]; (c) 34 nL of anthracene in pC8PryC1 FSA at 150 mM by inkjet printing (frequency: 120 Hz, pulse width: 75 μs, head temperature: 40 °C, applied voltage: 55 V, number of ejections: 65); and (d) after heating at a heating rate of 1.0 °C min^{-1} to 57 °C.

Fig. 4 Dissolution temperatures of anthracene in pC8PryC1 FSA at 150 mM plotted against heating rates. The volumes of pC8PryC1 FSA were 0.5 mL and 34 nL for the conventional (gray circle) and inkjet (blue square) techniques, respectively. The dissolution temperature was the temperature at which the crystals were completely dissolved during observation with the unaided eye using the conventional technique or with a microscope using the inkjet technique.

optical microscope image of anthracene in DCB on the substrate immediately after ejection. The diameter of the anthracene solution on the substrate was *ca.* 0.86 mm. The droplet size decreased even during observation because of DCB evaporation. The droplets were uniform and transparent, with no precipitates observed.

Fig. 3b shows an optical microscope image of anthracene after the DCB was dried. Anthracene crystals precipitated where the droplet had been. Fig. 3c shows an optical microscope image of anthracene crystals covered with pC8PryC1 FSA at 34 nL to prepare the anthracene solution at 150 mM. The shape of the droplet was slightly distorted because each droplet of the ionic liquid was dispensed manually at different locations of the substrate to completely cover the anthracene crystals. The diameter of the ionic liquid droplet was *ca.* 0.72 mm. Large crystals were evident, and some small crystals were dissolved in the ionic liquid.

As the temperature was increased at a heating rate of 1 °C min^{-1}, the crystals dissolved gradually. The crystals dissolved completely at 57 °C (Fig. 3d). This was defined as the dissolution temperature at 150 mM. Note that the anthracene completely dissolved when the ionic liquid was ejected at a head temperature of 80 °C. A low temperature of the ionic liquid ejection facilitates the measurement of the dissolution temperature.

Heating rate for concentration and temperature equilibrium

The heating rate was studied to determine the dissolution temperature of anthracene in pC8PryC1 FSA at 150 mM. Fig. 4 shows the dis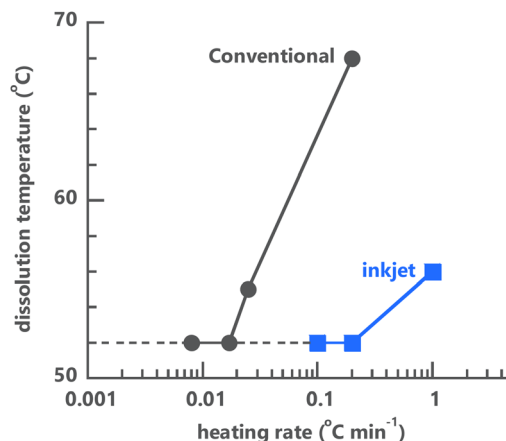solution temperatures of anthracene in the ionic liquid plotted against the heating rate measured by applying conventional (0.5 mL) and inkjet (34 nL) techniques. In the conventional technique, a heating rate of 0.2 °C min^{-1} corresponded to a dissolution temperature of 68 °C. The dissolution temperature decreased as the heating rate decreased. A heating rate < 0.017 °C min^{-1} corresponded to a constant dissolution temperature of 52 °C. This temperature was defined as the dissolution temperature at an equilibrium of 150 mM. In the inkjet technique, a heating rate of 1.0 °C min^{-1} corresponded to a dissolution temperature of 56 °C. A heating rate of <0.20 °C min^{-1} corresponded to a constant dissolution temperature of 52 °C. This dissolution temperature was consistent with that obtained using the conventional technique. The heating rate of the inkjet at which the dissolution temperature was obtained was 10× faster than that of the conventional technique. This was because temperature and concentration equilibriums were reached quickly (because of the small size of the droplets).

Fig. S1† shows optical microscope images to obtain dissolution conditions at 50 mM of 9,10-dibromoanthracene in 0.5 nL of pC8PryC1 TFSA at a heating rate of 0.17 °C min^{-1}. The dissolution temperature was about 100 °C, which was almost the same as that obtained using the conventional technique. This new technique can also be used for other anthracene derivatives and pyridinium derivatives.

Phase diagram obtained using the inkjet technique

Phase diagrams were prepared for anthracene in pC8PryC1 FSA by applying the inkjet and conventional techniques at the optimized heating rates (Fig. 5 and S2†). The phase diagram obtained by applying the conventional technique corresponded to dissolution temperatures of 35 °C, 52 °C, and 62 °C at 75, 150, and 300 mM, respectively. The phase diagram obtained by applying the inkjet technique exhibited good agreement with this result. The heating rate at 0.2 °C min^{-1} in the inkjet
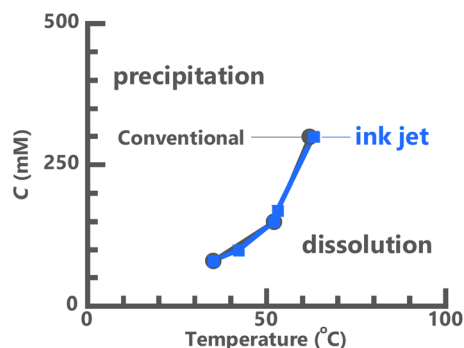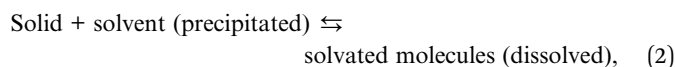
Fig. 5 Phase diagrams of anthracene in pC8PryC1 FSA by applying the inkjet (blue square) and conventional (gray circle) techniques, at pC8PryC1 FSA volumes of 25–100 nL and 0.5–1.0 mL, respectively, at heating rates of 0.20 °C min^{-1} and 0.017 °C min^{-1}, respectively. Anthracene solutions and pC8PryC1 FSA were ejected under the optimized conditions depicted in Fig. 3.

technique was sufficiently slow to reach concentration and temperature equilibrium at each concentration. The solubility curves remained unchanged when the solution volume was reduced from milliliters in the conventional approach to nanoliters in the inkjet approach.

The solubility increased proportionally to the temperature. This tendency was called "the upper critical solution phenomena". The solubility curves allow the calculation of solubility enthalpy and dissolution entropy by the van't Hoff equation (eqn (1)) assuming an equilibrium state of the solute (eqn (2)):[39]

$$C_e = d \exp\left(-\frac{\Delta_d H}{R}\frac{1}{T} - \frac{\Delta_d S}{R}\right), \quad (1)$$

Solid + solvent (precipitated) $\leftrightarrows$

solvated molecules (dissolved), (2)

where C_e is the equilibrium concentration of the anthracene derivatives in the solution (mol L^{-1}); d is the molar density of the anthracene derivatives in the crystal (7.103 mol L^{-1}); $\Delta_d H$ and $\Delta_d S$ are dissolution enthalpy and entropy (J mol^{-1}), respectively; T is the absolute temperature (K); and R is the gas constant (8.314 J mol^{-1} K^{-1}). The $\Delta_d H$ and $\Delta_d S$ were calculated from the phase diagram and the above eqn (1) to be +41 kJ mol^{-1} and +94 J mol^{-1} K^{-1}, respectively, which were almost equal to those obtained by applying conventional techniques.[38] These thermodynamic constants led to a continuous relationship between concentration and temperature. In addition, these provide guidelines for material design regarding solubility because enthalpy and entropy represent intermolecular interactions and the degree of freedom of molecule arrangements. The more important point is that the supersaturation degree can be determined quantitatively. The supersaturation degree ΔC (>0) is calculated by subtracting the concentration C_e of the saturated solutions from the C_s of the supersaturated solutions. The supersaturation degree is an important factor to quantitatively determine nucleation frequency and crystal growth rate, which are generally proportional to ΔC^{2-} and ΔC_{1-2}, respectively.

Variation in the dissolution temperature of each droplet

The dissolution temperatures were concomitantly measured in nine droplets (35 nL and 150 mM) on substrates prepared by inkjet printing. The droplet-patterned density was approximately 51.5 dots per cm^2. Fig. 6 shows optical microscope
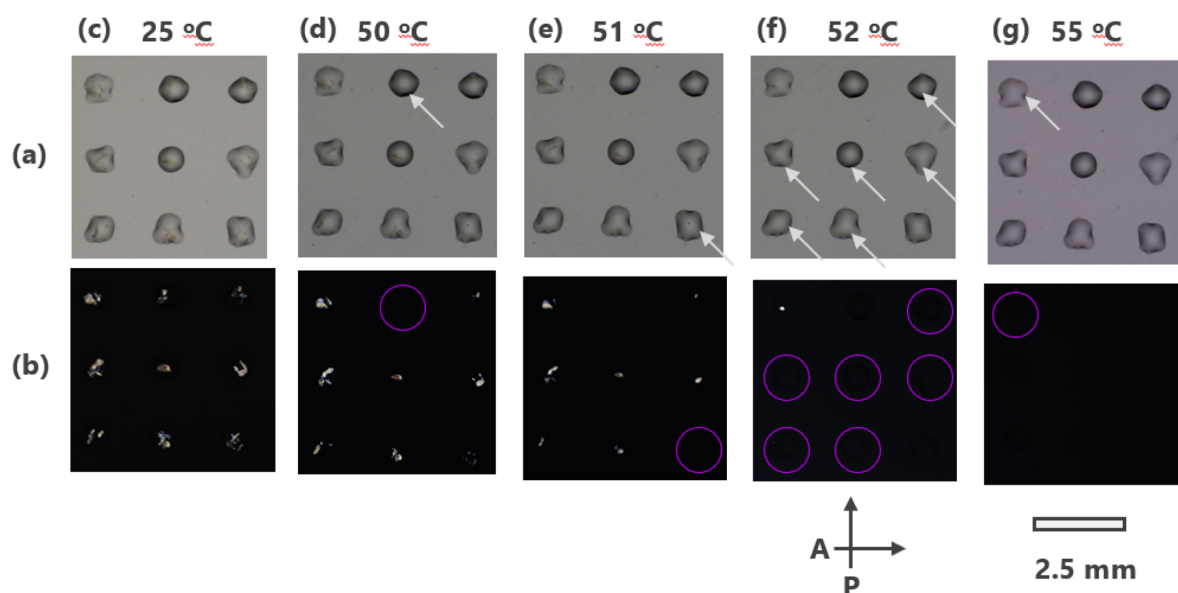

Fig. 6 Optical microscope images in (a) bright field and (b) cross-Nicol mode of anthracene crystals in pC8PryC1 FSA droplets, at 35 nL and 150 mM, printed using the inkjet technique. Anthracene solutions and pC8PryC1 FSA were ejected onto a glass substrate at (c) 25 °C under the optimized conditions illustrated in Fig. 3. The sample was heated at a rate of 0.20 °C min^{-1}. Parts (d–g) show images at 50 °C, 51 °C, 52 °C, and 55 °C, respectively. Gray arrows and purple circles indicate the droplets in which anthracene dissolved completely. The characters A (analyzer) and P (polarizer) indicate the direction of the polarized light.

Table 1 Comparison between the conventional and our techniques

	Conventional	This study
Solvent	Volatile	Non-volatile
Preparation of solutions	Vial and pipet only	Inkjet printer
Observation	Eye	Optical microscope
Volume of sample (liter)	10^{-1} to 10^{-3}	10^{-6} to 10^{-12}
Weight of solute (gram)	10^{-1} to 10^{-3}	10^{-6} to 10^{-12}
Measuring time	Weeks–months	Hours–days
Number of samples at the same time (cm^{-2})	1–2	1–1 000 000

images in (a) a bright field and (b) crossed-Nicol mode obtained from the samples at (c) 25 °C, (d) 50 °C, (e) 51 °C, (f) 52 °C, and (g) 55 °C at a heating rate of 0.2 °C min^{-1}. The crossed-Nicol images indicate the presence of anthracene crystals with high contrast. Parts (a) and (b) in Fig. 6 indicate that anthracene crystals were present in each droplet. The crystals gradually dissolved as the temperature increased. At 50 °C and 51 °C, the anthracene crystals in the droplet marked with a purple circle dissolved completely (parts (d) and (e) in Fig. 6). The dissolution temperatures of this droplet were 50 °C and 51 °C, respectively. At 52 °C, the anthracene crystals in droplets dissolved completely (part (f) in Fig. 6). The dissolution temperature of the six droplets was 51 °C. The dissolution temperature of the remaining droplet was 55 °C (part (g) in Fig. 6). The average and standard deviation of the dissolution temperatures were 52.1 °C and 0.8 °C (2.5%), respectively. This standard deviation is smaller than those of the ejected volumes of the anthracene solution and ionic liquid.

Conclusions

We demonstrate a combinatorial analysis method to obtain concentration–temperature phase diagrams of anthracene derivatives in pC8PryC1 derivatives on substrates printed by applying the inkjet technique. A volume of 0.5 nL of the anthracene solution and ionic liquid was ejected with standard deviations of 0.3% and 7%, respectively. The solution was ejected for anthracene and pC8PryC1 FSA at the applied as the applied voltage 20 and 55 V, the applied frequency of 500 and 120 Hz, and head temperature 30 °C and 40 °C, respectively. Nanoliter droplets (diameter: *ca.* 1 mm) were placed at a droplet-patterned density of *ca.* 50 dots per cm^2. The dissolution temperature of anthracene at each concentration was obtained at a heating rate of 0.2 °C min^{-1}. The standard deviation of the dissolution temperatures was 0.8 °C (2.5%). This technique also worked for 9,10-dibromoanthracene in pC8PryC1 TFSA.

Table 1 summarizes the comparison between the conventional technique and this technique. This technique uses small quantities of reagents and solvents, requires a brief time, and enables multiple simultaneous measurements of many samples. The advantage of using only a small quantity of reagents facilitates the analysis of phase diagrams of valuable reagents, such as nucleic acid drugs, proteins, and synthesized compounds. Small droplets enable precise and accurate solubility analysis by microscopy and in-site analysis, such as optical spectroscopy, electrochemistry, and calorimetry. For quantitative spectrum measurements, it should be necessary to devise ways to determine the optical path of the droplet solutions.

Simultaneous measurements of many samples in a short time enable screening of many solute and solvent combinations and performing crystal engineering based on phase diagrams. Even with commercially available inkjet printers, the diameter can be reduced to micrometers (droplet volume: picolitres). This further optimizes droplet density and measurement time. Other solutes and ionic liquids can also be used. Note that the properties of ionic liquids, such as non-volatility, high viscosity, and high salt strength, could lead to some disadvantages. For example, it might not be suitable for picking crystals up without ionic liquids, for rapid crystal growth in droplets, or for analysing multivalent ion materials. However, these disadvantages also have the potential for new crystal engineering, such as composites between ionic liquids and crystals, suppression of unwanted crystallization, and discovery of new combinations of solvents and solutes. This technique will facilitate open microsystem research in combinatorial science, microsystems, crystal engineering, physical chemistry, and ionic liquid science.

Data availability

The data supporting this article have been included as part of the ESI.†

Author contributions

S. Watanabe proposed and conducted this research, S. Inouch performed all the experiments, and M. Kunitake advised for this research.

Conflicts of interest

The authors declare no conflicts of interest associated with this manuscript.

Acknowledgements

References

1 T. Izawa, E. Miyazaki and K. Takimiyas, *Adv. Mater.*, 2008, **20**, 3388–3392.

2 M. Hoshino, A. Khutia, H. Xing, Y. Inokuma and M. Fujita, *IUCrJ*, 2016, **3**, 139–151.

3 Y. Inokuma, S. Yoshioka, J. Ariyoshi, T. Arai, Y. Hitora, K. Takada, S. Matsunaga, K. Rissanen and M. Fujita, *Nature*, 2013, **495**, 461–466.

4 C. G. Jones, M. Asay, L. J. Kim, J. F. Kleinsasser, A. Saha, T. J. Fulton, K. R. Berkley, D. Cascio, A. G. Malyutin, M. P. Conley, B. M. Stoltz, V. Lavallo, J. A. Rodríguez and H. M. Nelson, *ACS Cent. Sci.*, 2019, **5**, 1507–1513.

5 C. G. Jones, M. W. Martynowycz, J. Hattne, T. J. Fulton, B. M. Stoltz, J. A. Rodriguez, H. M. Nelson and T. Gonen, *ACS Cent. Sci.*, 2018, **4**, 1587–1592.

6 R. Medishetty, A. Husain, Z. Bai, T. Runčevski, R. E. Dinnebier, P. Naumov and J. J. Vittal, *Angew. Chem., Int. Ed.*, 2014, **53**, 5907–5911.

7 S. Kobatake, S. Takami, H. Muto, T. Ishikawa and M. Irie, *Nature*, 2007, **446**, 778–781.

8 A. G. Marangoni and S. E. McGauley, *CrystEngComm*, 2003, **3**, 95–108.

9 R. L. Wille and E. S. Lutton, *J. Am. Oil Chem. Soc.*, 1966, **43**, 491–496.

10 A. Grunenberg, J. O. Henck and H. W. Siesler, *Int. J. Pharm.*, 1996, **129**, 147–158.

11 N. Blagden, M. de Matas, P. T. Gavan and P. York, *Adv. Drug Delivery Rev.*, 2007, **59**, 617–630.

12 S. J. Pearton, J. C. Zolper, R. J. Shul and F. Ren, *J. Appl. Phys.*, 1999, **86**, 1–78.

13 H. Hoppe and N. S. Sariciftci, *J. Mater. Res.*, 2004, **19**, 1924–1945.

14 D. Shi, V. Adinolfi, R. Comin, M. Yuan, E. Alarousu, A. Buin, Y. Chen, S. Hoogland, A. Rothenberger, K. Katsiev, Y. Losovyj, X. Zhang, P. A. Dowben, O. F. Mohammed, E. H. Sargent and O. M. Bakr, *Science*, 2015, **347**, 519–522.

15 S. Watanabe, T. Fujita, J. C. Ribierre, K. Takaishi, M. Uchiyama, C. Adachi, T. Muto, T. Aoyama and M. Matsumoto, *ACS Appl. Mater. Interfaces*, 2016, **8**, 17574–17582.

16 J. C. Ribierre, L. Zhao, S. Furukawa, T. Kikitsu, D. Inoue, A. Muranaka, K. Takaishi, T. Muto, S. Matsumoto, D. Hashizume, M. Uchiyama, P. André, C. Adachi and T. Aoyama, *Chem. Commun.*, 2015, **51**, 5836–5839.

17 M. S. Sanjiv, *Int. J. Res. Appl. Sci. Eng. Technol.*, 2022, **10**, 433–450.

18 J. R. Luft, J. Newman and E. H. Snell, *Acta Crystallogr., Sect. F:Struct. Biol. Cryst. Commun.*, 2014, **70**, 835–853.

19 S. Watanabe, T. Ohta, R. Urata, T. Sato, K. Takaishi, M. Uchiyama, T. Aoyama and M. Kunitake, *Langmuir*, 2017, **33**, 8906–8913.

20 S. Watanabe, R. Urata, T. Sato, S. Ida and M. Kunitake, *Cryst. Growth Des.*, 2019, **19**, 3410–3416.

21 B. Zheng and R. F. Ismagilov, *Angew. Chem., Int. Ed.*, 2005, **44**, 2520–2523.

22 I. Barbulovic-Nad, S. H. Au and A. R. Wheeler, *Lab Chip*, 2010, **10**, 1536–1542.

23 M. J. Jebrail, M. S. Bartsch and K. D. Patel, *Lab Chip*, 2012, **12**, 2452–2463.

24 P. Paik, V. K. Pamula and R. B. Fair, *Lab Chip*, 2003, **3**, 253–259.

25 M. B. Nagarajan, A. M. Tentori, W. C. Zhang, F. J. Slack and P. S. Doyle, *Microsyst. Nanoeng.*, 2020, **6**, 51.

26 S. L. Morissette, Ö. Almarsson, M. L. Peterson, J. F. Remenar, M. J. Read, A. V. Lemmo, S. Ellis, M. J. Cima and C. R. Gardner, *Adv. Drug Delivery Rev.*, 2004, **56**, 275–300.

27 J. Jancarik and S. H. Kim, *J. Appl. Crystallogr.*, 1991, **24**, 409–411.

28 Y. Zhu, L. N. Zhu, R. Guo, H. J. Cui, S. Ye and Q. Fang, *Sci. Rep.*, 2014, **4**, 5046.

29 T. Di Zhang, L. L. Chen, W. J. Lin, W. P. Shi, J. Q. Wang, C. Y. Zhang, W. H. Guo, X. Deng and D. C. Yin, *Appl. Microbiol. Biotechnol.*, 2021, **105**, 2759–2773.

30 B. Zheng, L. S. Roach and R. F. Ismagilov, *J. Am. Chem. Soc.*, 2003, **125**, 11170–11171.

31 A. R. Tyler, R. Ragbirsingh, C. J. McMonagle, P. G. Waddell, S. E. Heaps, J. W. Steed, P. Thaw, M. J. Hall and M. R. Probert, *Chem*, 2020, **6**, 1755–1765.

32 W. E. Arter, R. Qi, N. A. Erkamp, G. Krainer, K. Didi, T. J. Welsh, J. Acker, J. Nixon-Abell, S. Qamar, J. Guillén-Boixet, T. M. Franzmann, D. Kuster, A. A. Hyman, A. Borodavka, P. S. George-Hyslop, S. Alberti and T. P. J. Knowles, *Nat. Commun.*, 2022, **13**, 7845.

33 Y. Takeyama, S. Maruyama and Y. Matsumoto, *Cryst. Growth Des.*, 2011, **11**, 2273–2278.

34 F. Qu, Q. Q. Zhu and C. L. Liu, *Cryst. Growth Des.*, 2014, **14**, 6421–6432.

35 S. Kato, Y. Takeyama, S. Maruyama and Y. Matsumoto, *Cryst. Growth Des.*, 2010, **10**, 3608–3611.

36 H. Jiang, Y. Cheng, Z. Wang, Z. Bai, Y. Tang, P. Sun, P. Wan and Y. Chen, *J. Electrochem. Soc.*, 2021, **168**, 016504.

37 M. Ito, Y. Yamashita, T. Mori, M. Chiba, T. Futae, J. Takeya, S. Watanabe and K. Ariga, *Langmuir*, 2022, **38**, 5237–5247.

38 S. Watanabe, K. Ono, R. Nakayama, K. Tajiri, S. Inouchi, T. Matsuo, M. Kunitake and S. Hayashi, *ChemPhysChem*, 2024, e202300867.

39 M. J. Jozwiakowski and K. A. Connors, *Carbohydr. Res.*, 1985, **143**, 51–60.